

Article

# Small-Signal Stability Research of Grid-Connected Virtual Synchronous Generators

Shengyang Lu <sup>1,2</sup>, Yu Zhu <sup>2</sup>, Lihu Dong <sup>1</sup>, Guangyu Na <sup>3</sup>, Yan Hao <sup>1</sup>, Guanfeng Zhang <sup>2</sup>, Wuyang Zhang <sup>2</sup>, Shanshan Cheng <sup>1</sup>, Junyou Yang <sup>1,\*</sup> and Yuqiu Sui <sup>1,3</sup>

<sup>1</sup> School of Electrical Engineering, Shenyang University of Technology, Shenyang 110870, China

<sup>2</sup> Electric Power Research Institute of State Grid Liaoning Electric Power Supply Co., Ltd., Shenyang 110006, China

<sup>3</sup> State Grid Liaoning Electric Power Supply Co., Ltd., Shenyang 110006, China

\* Correspondence: junyouyang@sut.edu.cn; Tel.: +86-139-4008-8191

**Abstract:** The virtual synchronous generator (VSG) technique is used to simulate the external characteristics of a synchronous generator (SG) to provide certain damping and inertia to power systems. However, it may easily cause low-frequency oscillation of the power system. We studied the small-signal stability of a grid-connected virtual synchronous generator. Firstly, the small-signal models of single-VSG and multi-VSG grid-connected systems were established. Subsequently, the system eigenvalues were obtained by solving the state matrix, and the system oscillation modes were analyzed. The eigenvalue analysis method was used to analyze the impacts of parameter changes, such as virtual moment of inertia, virtual damping coefficient, line resistance, and line inductance, on system stability. Finally, our conclusions were verified by numerous simulation models.

**Keywords:** virtual synchronous generator (VSG); low-frequency oscillation; small-signal model; stability analysis



**Citation:** Lu, S.; Zhu, Y.; Dong, L.; Na, G.; Hao, Y.; Zhang, G.; Zhang, W.; Cheng, S.; Yang, J.; Sui, Y. Small-Signal Stability Research of Grid-Connected Virtual Synchronous Generators. *Energies* **2022**, *15*, 7158. <https://doi.org/10.3390/en15197158>

Academic Editor: Mario Marchesoni

Received: 5 September 2022

Accepted: 23 September 2022

Published: 28 September 2022

**Publisher's Note:** MDPI stays neutral with regard to jurisdictional claims in published maps and institutional affiliations.



**Copyright:** © 2022 by the authors. Licensee MDPI, Basel, Switzerland. This article is an open access article distributed under the terms and conditions of the Creative Commons Attribution (CC BY) license (<https://creativecommons.org/licenses/by/4.0/>).

## 1. Introduction

Many new energy units are connected to the power system through inverters, and the proportion of power electronic devices in the power system has increased rapidly [1]. The operation mode and dynamic characteristics of the power grid have changed gradually [2–4]. A power system including fewer synchronous generators (SG) and more power electronic devices cannot provide sufficient physical damping and inertia, which is not conducive to the stable operation of the power system [5].

To solve the above problems, the virtual synchronous generator (VSG) technique is proposed [6,7]. The VSG considers the electromechanical and excitation transient characteristics of synchronous generators to provide virtual damping and inertia [8]. However, although VSG simulates the excellent regulation characteristics of SG, low-frequency oscillation problems will occur and the oscillation mode will be changed [9,10]. Therefore, the grid-connected stability of VSG needs to be further analyzed. In this regard, single-VSG and multi-VSG grid-connected stabilities are widely studied.

In the study of single-machine grid connection stability, Reference [11] developed a double-machine test-bed to analyze the low-frequency oscillation phenomenon after VSG replaces SG, as well as the characteristics and main modes of low-frequency oscillation, and evaluated the role of the power system stabilizer in the VSG grid. In [12], the internal voltage of the inverter was taken as a parameter rather than a state variable, and the voltage change was introduced into the approximate Lyapunov direct method. The influence of the reactive power voltage control link and different parameters on the stability of VSG was analyzed, and it was pointed out that the reactive power control loop will reduce the stability margin of the VSG power angle. Reference [13] proposed the concepts of virtual common coupling point and virtual power angle to represent the mathematical model of a variable cross-section vibration generator with virtual damping and analyzed the

transient stability of VSG. In [14], a small-signal model of a VSG-SG interconnected system suitable for studying the low-frequency oscillation damping of the transmission network is proposed. Through this model, the influence of VSG and SG on the power system is compared, and the mechanism of VSG's influence on damping characteristics is revealed. In [15], the VSG small-signal model of voltage and current double closed loop and active and reactive power control was established to study the VSG oscillation characteristics. The analysis showed that the reactive power loop and DQ axis voltage control have a great impact on the damping of low-frequency oscillation.

In the research on the stability of multi-machine parallel connection, in [16], the VSG-based active power frequency loop is equivalent to  $P/\omega$ . The two-terminal-network model of "admittance" analyzes the three kinds of factors that affect the output power of VSG and the power frequency oscillation characteristics of the three kinds of factors when the parameters change. Reference [17] defines the deviation of generator voltage angle relative to inertia center angle as a tool to evaluate the stability of a multi-VSG microgrid and optimizes VSG unit parameters through the particle swarm optimization algorithm. Reference [18] studies a new method to improve the transient stability of a multi-VSG power grid, which suppresses the oscillation between VSG and the inertial frequency center of the power grid during short circuit. Reference [19] proposes a fully decentralized mutual damping method to solve the problem of power oscillation in parallel with multiple VSGs. By introducing the derivative of local power, the difference between each angular frequency is obtained indirectly, which effectively suppresses power oscillation. In [20], secondary frequency control of a distributed VSG for low-bandwidth communication is proposed, which suppresses oscillation and restores the frequency to the rated value without changing the virtual inertia provided by VSG.

To summarize, the theory of VSG grid connection stability is gradually maturing, but the extant literature does not discuss the specific impact of the changes in various parameters in VSG on the low-frequency oscillation mode of the power system after VSG grid connection, as well as the dominant factors in the change in oscillation mode. Moreover, nowadays, the stability research on VSG control mostly adopts the damping torque analysis method. Although this method is easy to build a complex global model, its stability criteria are complex and the parameter regions are difficult to identify [21]. The eigenvalue analysis method in the small-signal analysis method can better analyze the stability of the system when the parameters change. Therefore, we present here a more in-depth study on the grid connection stability of a virtual synchronous generator based on the small-signal model analysis method. The influence of VSG parameters on the stability of a single-machine grid-connected system and a multi-machine grid-connected system is analyzed through system eigenvalue trajectories. The main contributions are as follows:

- (1) Based on the topology and algorithm of VSG, small-signal modeling is carried out for a single-machine grid-connected system and a multi-machine parallel grid-connected system.
- (2) In the single-machine grid-connected system, the influences of oscillation mode, control parameters of active power loop, and resistance inductance ratio of connecting line on eigenvalues are analyzed.
- (3) In the multi-machine parallel connected system, the effects of virtual moment of inertia, damping coefficient, line resistance, and line inductance on the eigenvalues are analyzed. Finally, the conclusions are verified by numerous simulation models.

## 2. VSG Control Strategy

### 2.1. VSG Topology

The topology of the virtual synchronous generator is shown in Figure 1. VSG can be divided into four layers. The first layer is the power loop controller, which is composed of an abc/dq transformation link and a power calculation module. The second layer is the VSG control algorithm, which is used to generate the voltage references. The third layer is the voltage and current double closed-loop controllers, which consist of voltage

and current double closed-loop modules and dq/abc transformation. The fourth layer is sinusoidal pulse width modulation.

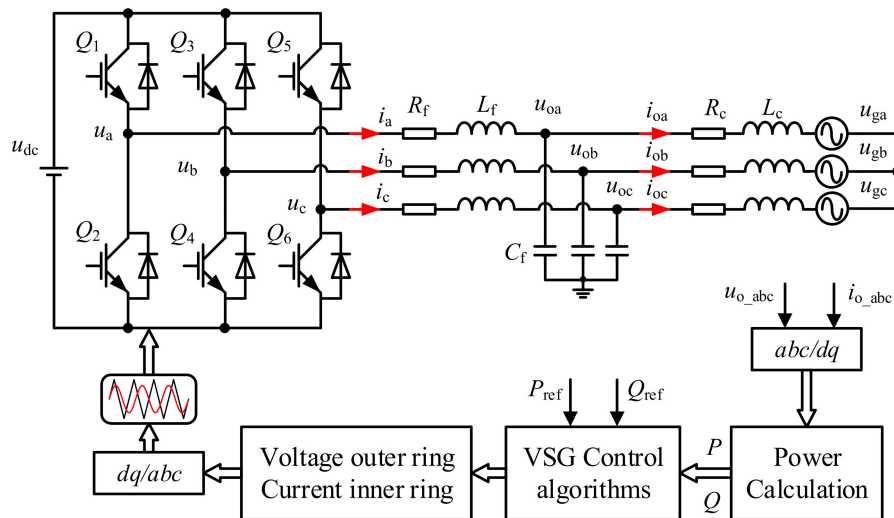


Figure 1. Topology diagram of VSG.

In Figure 1,  $u_{dc}$  is the ideal DC voltage on the DC side,  $R_f$  is resistance,  $L_f$  is inductance, and  $C_f$  is capacitance.  $R_c$  and  $L_c$  are the resistance and inductance of the connecting line.  $u_a$ ,  $u_b$ , and  $u_c$  are the output voltage of the inverter.  $i_a$ ,  $i_b$ , and  $i_c$  are the output currents of the inverter.  $i_{0a}$ ,  $i_{0b}$ , and  $i_{0c}$  are the currents of the line inductance.  $u_{0a}$ ,  $u_{0b}$ , and  $u_{0c}$  are the filter capacitor voltages.  $u_{ga}$ ,  $u_{gb}$ , and  $u_{gc}$  are the AC power grid voltages.  $P_{ref}$  is the active power, and  $Q_{ref}$  is the reactive power.

2.2. VSG Algorithm

2.2.1. Virtual Power Frequency Controller

To realize the simulation of the synchronous generator governor, the virtual speed regulator in VSG usually adopts frequency droop control to realize primary frequency regulation, and its control structure is shown in Figure 2.

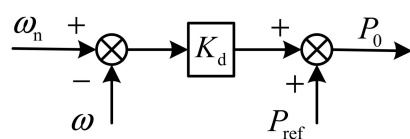


Figure 2. Structure block diagram of VSG governor control.

In Figure 2,  $\omega_n$  is the rated angular frequency of VSG,  $\omega$  is the output virtual angular frequency,  $K_d$  is the active frequency regulation coefficient of the governor, and  $P_0$  is the mechanical power.

As we know, the inertia and damping characteristics are mainly controlled by the mechanical rotational inertia of the rotor, which are transient regulation characteristics. The adequate damping can suppress overshoot and oscillations of output. The virtual moment of inertia control in VSG is shown in Figure 3.

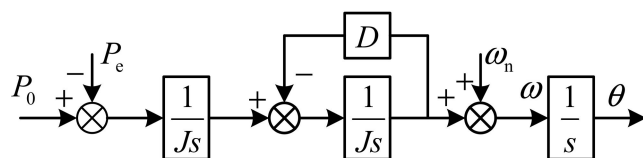


Figure 3. Structure of virtual moment of inertia control.

In Figure 3,  $J$  is the VSG virtual moment of inertia,  $D$  is the VSG virtual damping coefficient,  $P_e$  is the electromagnetic power, and  $\theta$  is the electrical angle.

### 2.2.2. Virtual Excitation Controller

The virtual excitation regulator in VSG adopts reactive voltage droop control to realize the voltage regulation characteristics of the excitation system of SG. The block diagram of VSG virtual excitation control is shown in Figure 4.

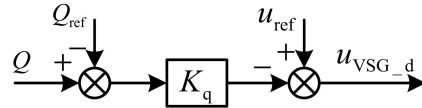


Figure 4. The block diagram of virtual excitation control.

In Figure 4,  $K_q$  is the reactive voltage regulation coefficient of the excitation controller, and  $u_{ref}$  is the reference voltage at the given point.

## 3. Small-Signal Model of Single-VSG Grid-Connected System

### 3.1. Small-Signal Model of Filter and Connecting Line

Assuming that the output voltage of the inverter can accurately track the reference, ignoring the switching delay and loss of power electronic devices, combined with the VSG topology shown in Figure 1, the state equations of the filter and the connecting line are obtained according to the basic circuit laws.

$$\begin{cases} \frac{di_d}{dt} = \frac{1}{L_f}(-R_f i_d + \omega L_f i_q + u_d - u_{od}) \\ \frac{di_q}{dt} = \frac{1}{L_f}(-R_f i_q - \omega L_f i_d + u_q - u_{oq}) \\ \frac{du_{od}}{dt} = \frac{1}{C_f}(\omega C_f u_{oq} + i_d - i_{od}) \\ \frac{du_{oq}}{dt} = \frac{1}{C_f}(-\omega C_f u_{od} + i_q - i_{oq}) \\ \frac{di_{od}}{dt} = \frac{1}{L_c}(\omega L_c i_{oq} + u_{od} - u_{bd} - R_c i_{od}) \\ \frac{di_{oq}}{dt} = \frac{1}{L_c}(-\omega L_c i_{od} + u_{oq} - u_{bq} - R_c i_{oq}) \end{cases}, \quad (1)$$

where  $u_d, u_q, i_d,$  and  $i_q$  are dq axis components of output voltages and currents of the grid-connected inverter;  $u_{od}$  and  $u_{oq}$  are dq axis components of filter capacitor voltage;  $i_{od}$  and  $i_{oq}$  are dq axis components of inductance  $L_c$  current; and  $u_{gd}$  and  $u_{gq}$  are dq axis components of AC grid voltage.

The small-signal model of the filter and connecting line is:

$$\frac{d}{dt} \begin{bmatrix} \Delta i_{dq} \\ \Delta u_{odq} \\ \Delta i_{odq} \end{bmatrix} = A_f \begin{bmatrix} \Delta i_{dq} \\ \Delta u_{odq} \\ \Delta i_{odq} \end{bmatrix} + B_{f1} [\Delta u_{dq}] + B_{f2} [\Delta u_{gdq}] + B_{f3} [\Delta \omega], \quad (2)$$

where

$$A_f = \begin{bmatrix} -\frac{R_f}{L_f} & \omega_0 & -\frac{1}{L_f} & 0 & 0 & 0 \\ -\omega_0 & -\frac{R_f}{L_f} & 0 & -\frac{1}{L_f} & 0 & 0 \\ \frac{1}{C_f} & 0 & 0 & \omega_0 & -\frac{1}{C_f} & 0 \\ 0 & \frac{1}{C_f} & -\omega_0 & 0 & 0 & -\frac{1}{C_f} \\ 0 & 0 & \frac{1}{L_c} & 0 & \frac{R_c}{L_c} & \omega_0 \\ 0 & 0 & 0 & \frac{1}{L_c} & -\omega_0 & \frac{R_c}{L_c} \end{bmatrix}, B_{f1} = \begin{bmatrix} -\frac{1}{L_f} & 0 \\ 0 & -\frac{1}{L_f} \\ 0 & 0 \\ 0 & 0 \\ 0 & 0 \\ 0 & 0 \end{bmatrix}, B_{f2} = \begin{bmatrix} 0 & 0 \\ 0 & 0 \\ 0 & 0 \\ 0 & 0 \\ -\frac{1}{L_c} & 0 \\ 0 & -\frac{1}{L_c} \end{bmatrix}, B_{f3} = \begin{bmatrix} I_q \\ -I_d \\ U_{oq} \\ -U_{od} \\ I_{oq} \\ -I_{od} \end{bmatrix}.$$

### 3.2. Small-Signal Models of Power Calculation and VSG Control Algorithm

The small-signal model of instantaneous power calculation is obtained by (3).

$$\begin{cases} \Delta P = 1.5(I_{od}\Delta v_{od} + I_{oq}\Delta v_{oq} + V_{od}\Delta i_{od} + V_{oq}\Delta i_{oq}) \\ \Delta Q = 1.5(-I_{oq}\Delta v_{od} + I_{od}\Delta v_{oq} + V_{oq}\Delta i_{od} - V_{od}\Delta i_{oq}) \end{cases} \quad (3)$$

According to the power frequency and the excitation controllers, the state equation of the VSG control algorithm is shown in (4).

$$\begin{cases} J \frac{d(\omega_n - \omega)}{dt} = \frac{P - P_{ref} - K_d(\omega_n - \omega)}{\omega_n} - D(\omega_n - \omega) \\ u_{VSG\_d} = u_{ref} - K_q(Q - Q_{ref}) \end{cases} \quad (4)$$

Linearizing Equation (4), the small-signal model of the VSG control algorithm is obtained by (5).

$$\begin{cases} \frac{d\Delta\omega}{dt} = -\frac{K_d + D\omega_n}{J\omega_n} \Delta\omega - \frac{1}{J\omega_n} \Delta P \\ \Delta u_{VSG\_d} = -K_q \Delta Q \end{cases} \quad (5)$$

### 3.3. Small-Signal Model of Voltage and Current Closed Loops

Figure 5 shows the control structure of the voltage outer loop and the current inner loop. In Figure 5,  $K_{pv}$ ,  $K_{iv}$ ,  $K_{pc}$ , and  $K_{ic}$  are the PI controller parameters of the voltage outer loop and the current inner loop, respectively.

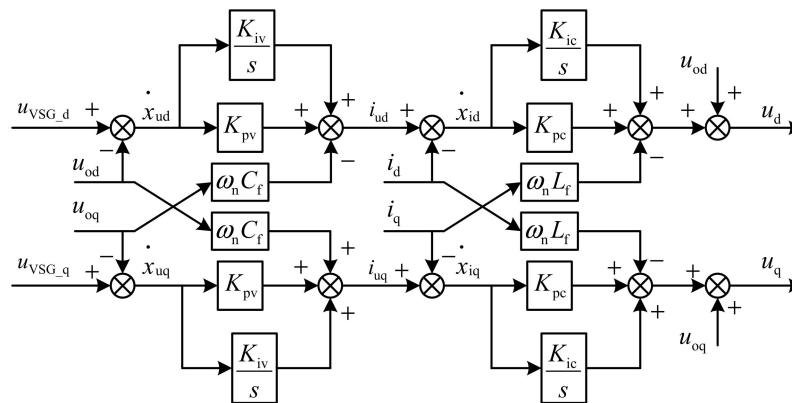


Figure 5. Block diagram of voltage–current double-loop control.

According to Figure 5, the small-signal model of voltage and current closed loops is expressed by (6).

$$\begin{cases} \Delta i_{ud} = K_{iv}\Delta x_{ud} + K_{pv}\Delta u_{VSG\_d} - K_{pv}\Delta u_{od} - \omega_n C_f \Delta u_{oq} \\ \Delta i_{uq} = K_{iv}\Delta x_{uq} + K_{pv}\Delta u_{VSG\_q} - K_{pv}\Delta u_{oq} + \omega_n C_f \Delta u_{od} \\ \Delta u_d = K_{ic}\Delta x_{id} + K_{pc}\Delta i_{ud} - K_{pc}\Delta i_d - \omega_n L_f \Delta i_q + \Delta u_{od} \\ \Delta u_q = K_{ic}\Delta x_{iq} + K_{pc}\Delta i_{uq} - K_{pc}\Delta i_q + \omega_n L_f \Delta i_d + \Delta u_{oq} \end{cases} \quad (6)$$

where  $x_{ud}$ ,  $x_{uq}$ ,  $x_{id}$ , and  $x_{iq}$  are the intermediate state variables to describe the dynamic characteristics of PI controller in voltage and current closed loops. The corresponding state equation is calculated by (7).

$$\begin{cases} \frac{dx_{ud}}{dt} = u_{VSG\_d} - u_{od} \\ \frac{dx_{uq}}{dt} = u_{VSG\_q} - u_{oq} \\ \frac{dx_{id}}{dt} = i_{ud} - i_d \\ \frac{dx_{iq}}{dt} = i_{uq} - i_q \end{cases} \quad (7)$$

The small-signal model is summarized by (8).

$$\frac{d}{dt} \begin{bmatrix} \Delta x_{udq} \\ \Delta x_{idq} \end{bmatrix} = A_1 \begin{bmatrix} \Delta u_{odq} \\ \Delta i_{dq} \end{bmatrix} + B_1 \begin{bmatrix} \Delta i_{dq} & \Delta u_{odq} & \Delta i_{odq} \end{bmatrix}^T, \tag{8}$$

where

$$A_1 = \begin{bmatrix} 1 & 0 & 0 & 0 \\ 0 & 1 & 0 & 0 \\ 0 & 0 & 1 & 0 \\ 0 & 0 & 0 & 1 \end{bmatrix}, B_1 = \begin{bmatrix} 0 & 0 & -1 & 0 & 0 & 0 \\ 0 & 0 & 0 & -1 & 0 & 0 \\ -1 & 0 & 0 & 0 & 0 & 0 \\ 0 & -1 & 0 & 0 & 0 & 0 \end{bmatrix}.$$

### 3.4. Small-Signal Model of Power Grid

The grid voltage and frequency are modeled by (9).

$$\begin{cases} u_{gd} = E_g \sin \delta_g \\ u_{gq} = E_g \cos \delta_g \\ \dot{\delta}_g = \omega_g - \omega \end{cases}, \tag{9}$$

where  $E_g$  is the voltage amplitude of the AC power grid,  $\omega_g$  is the angular frequency of the AC power grid, and  $\delta_g$  is the phase difference between the AC grid voltage and the d axis of the reference coordinate system.

Linearizing Equation (9), the small-signal model of the power grid is shown in (10).

$$\begin{cases} \Delta u_{gd} = E_g \cos \delta_{g0} \Delta \delta_g \\ \Delta u_{gq} = -E_g \sin \delta_{g0} \Delta \delta_g \\ \Delta \dot{\delta}_g = -\Delta \omega \end{cases}. \tag{10}$$

Based on the above small-signal models, the overall small-signal model of the single VSG grid-connected system can be obtained by (11).

$$\Delta \dot{x} = A \Delta x, \tag{11}$$

where  $\Delta x = [\Delta x_1, \Delta \delta_g]^T$  is the system state variable, and  $\Delta x_1 = [\Delta \omega, \Delta i_{dq}, \Delta u_{odq}, \Delta i_{odq}, \Delta x_{udq}, \Delta x_{idq}]^T$ .

## 4. Small-Signal Model of Multi-VSG Grid-Connected System

For a multi-VSG grid-connected system, it is necessary to transform the coordinate system of all VSGs to a common coordinate system. For the convenience of analysis, the dq coordinate system of the first VSG is selected as the system common reference coordinate system, and the transformation diagrams of other VSGs are shown in Figure 6. We assume that the output voltage of the  $i$ -th VSG is ahead of that of the first VSG electrical angle  $\theta_i$ , as shown in (12).

$$\theta_i = \int (\omega_i - \omega_1) dt. \tag{12}$$

The following is the corresponding linearized equation of (12):

$$\Delta \dot{\theta}_i = \Delta \omega_i - \Delta \omega_1. \tag{13}$$

Thus, the small-signal output current  $\Delta i_{oDQ_i}$  of the  $i$ -th inverter on the common coordinate system and the output voltage  $\Delta u_{bdqi}$  on its own coordinate system can be obtained by Equations (14) and (15), respectively.

$$\Delta i_{oDQ_i} = T_{si} \Delta i_{odqi} + T_{ci} \Delta \theta_i. \tag{14}$$

$$\Delta u_{bdqi} = T_{si}^{-1} \Delta u_{bDQ_i} + T_{ui}^{-1} \Delta \theta_i. \tag{15}$$

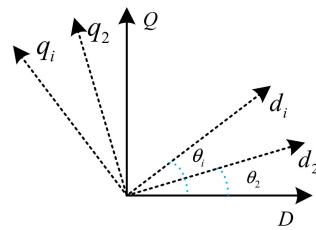


**Figure 6.** Schematic diagram of reference coordinate system transformation of multi-VSG system.

According to the transformation of the reference coordinate system, the small-signal model of the multi-VSG system is expressed by (16).

$$\Delta \dot{x}_i = A_i \Delta x_i, \quad (16)$$

where  $\Delta x_i = [\Delta x_1, \theta_2, \Delta x_1, \dots, \theta_i, \Delta x_i, \Delta \delta_g]^T$ .

## 5. Stability Analysis Based on Eigenvalues

### 5.1. Stability Analysis of Single-VSG Grid-Connected System

#### 5.1.1. Oscillation Mode Analysis of Single-VSG System

According to the single-VSG grid-connected small-signal model in Equation (11), all eigenvalues of the system are obtained based on the parameters in Tables 1 and 2. Subsequently, the oscillation mode of the single-VSG grid-connected system and the influence of parameter changes at the steady-state operation point on the small-signal stability of the system are analyzed.

**Table 1.** Single-VSG system parameters.

Parameter	Value	Parameter	Value
$R_f/\Omega$	0.2	$L_c/\text{mH}$	1.8
$L_f/\text{mH}$	3.2	$P_{\text{ref}}/\text{kW}$	10
$C_f/\mu\text{F}$	100	$Q_{\text{ref}}/\text{var}$	0
$R_c/\Omega$	0.1	$J/\text{kg}\cdot\text{m}^2$	10
$D/\text{N}\cdot\text{m}\cdot\text{s}\cdot\text{rad}^{-1}$	70	$K_d$	30
$K_q$	0.0005		

**Table 2.** Steady-state operating points of the single-VSG system.

Parameter	Value	Parameter	Value
$I_d/\text{A}$	21.27	$I_{\text{od}}/\text{A}$	1.8
$I_q/\text{A}$	11.66	$I_{\text{oq}}/\text{A}$	10
$U_{\text{od}}/\text{V}$	311.3	$\omega_0/\text{rad}\cdot\text{s}^{-1}$	314.2
$U_{\text{oq}}/\text{V}$	4.401		

The system eigenvalues are shown in Table 3. The system has twelve eigenvalues, corresponding to six oscillation modes. The eigenvalues of the system are in the left half plane of the complex plane, indicating that the system is stable. The distance between the eigenvalues  $\lambda_{11-12}$  and the imaginary axis is much greater than other eigenvalues, which has little influence on the system stability and can be ignored. The eigenvalues  $\lambda_{1-2}$  have the smallest oscillation frequency and are closest to the imaginary axis. An oscillation attenuation mode is presented for the system.

The following mainly considers the influence of active power outer loop controller parameters and connecting line parameters on system stability, especially the influence of virtual moment of inertia and virtual damping coefficient on system small-signal stability.

**Table 3.** Single-VSG system eigenvalues.

Eigenvalue	Real Part	Imaginary Part	Oscillation Frequency/Hz	Damping Ratio	Dominant Related State Variables
$\lambda_{1-2}$	-3.15	$\pm 6.89$	1.09	0.42	$i_d, i_q, x_{ud}, x_{uq}$
$\lambda_{3-4}$	-30.21	$\pm 22.38$	3.56	0.80	$i_d, i_q, x_{id}, x_{iq}$
$\lambda_{5-6}$	-6.84	$\pm 39.03$	6.21	0.17	$\omega, \delta_g,$
$\lambda_{7-8}$	-418.3	$\pm 349.98$	55.73	0.77	$i_{od}, i_{oq}$
$\lambda_{9-10}$	-217.04	$\pm 4797.2$	763.89	0.045	$i_d, i_q, u_{od}, u_{oq}$
$\lambda_{11-12}$	-1000	$\pm 5525.8$	879.90	0.18	$i_d, i_q, u_{od}, u_{oq}$

### 5.1.2. Influence of Active Power Loop Control Parameters on Eigenvalues

The control parameters of active power loop include the virtual moment of inertia  $J$  and the virtual damping coefficient  $D$ . The eigenvalue trajectories with the parameter changes are shown in Figure 7.

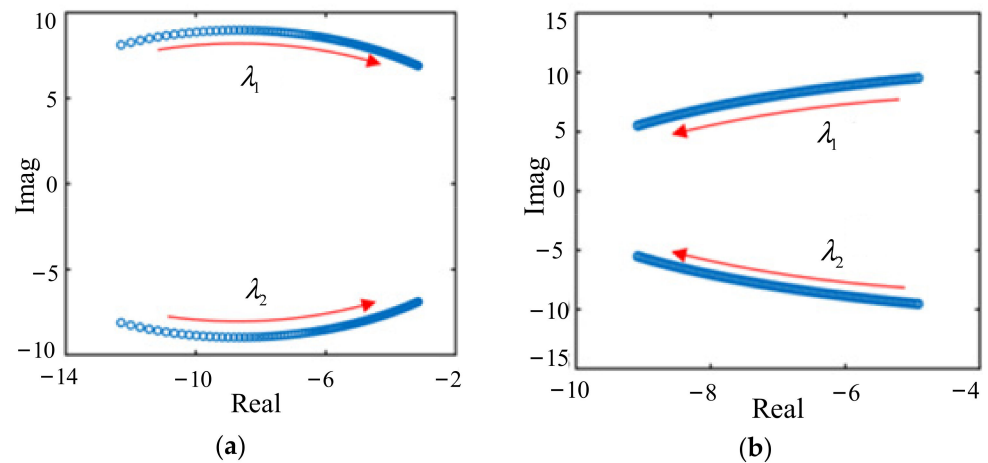


**Figure 7.** The eigenvalue trajectories under different active power control parameters. (a) Eigen-value trajectories of the system under different inertias. (b) Eigenvalue trajectories of the system under different damping coefficients.

When the virtual inertia changes  $J = 3.5 \rightarrow 14$ , other parameters remain unchanged, and the influence on the eigenvalues  $\lambda_{1-2}$  of the oscillation attenuation mode is shown in Figure 7a. With the increase in virtual inertia  $J$ , the eigenvalues  $\lambda_{1-2}$  move rapidly towards the imaginary axis, the damping ratios of the corresponding oscillation attenuation mode decrease rapidly, the oscillation frequency decreases slightly, and the system stability worsens. Shown in Figure 7b is the influence on the eigenvalues  $\lambda_{1-2}$  of the oscillation attenuation mode when the virtual damping coefficient changes  $D = 70 \rightarrow 130$ . With the increase in virtual damping coefficient  $D$ , the eigenvalues  $\lambda_{1-2}$  move to the left of the complex plane, and the movement speed away from the imaginary axis is much higher than that away from the real axis. The damping ratio of the corresponding oscillation attenuation mode increases, the overshoot will gradually decrease, the oscillation frequency will increase slightly, and the system stability will be improved.

### 5.1.3. Influence of Resistance Inductance Ratio of Connecting Line on Eigenvalues

The resistance inductance ratio  $r$  of the connecting line on the grid side is defined by (17).

$$r = \frac{R_c}{100\pi L_c}. \quad (17)$$

The resistance inductance ratio  $r$  of the connecting line on the grid side represents the voltage level of the grid. The influence of voltage level change on the eigenvalues is shown

in Figure 8. With the increase in  $r$ , the speed of the eigenvalues  $\lambda_{1-2}$  moving to the upper left of the coordinate system and away from the imaginary axis is much higher than that of the real axis, and the damping ratio of the system increases.

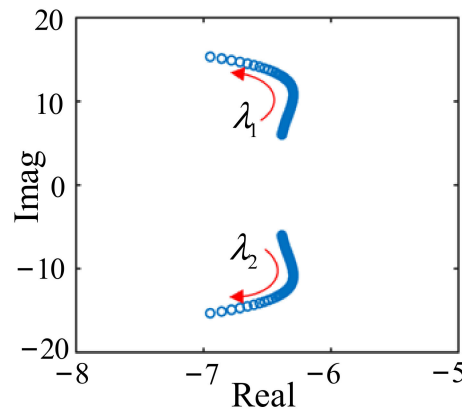


Figure 8. Eigenvalue trajectories under different resistance inductance ratios of connecting lines.

5.2. Stability Analysis of Multi-VSG System

5.2.1. Oscillation Mode Analysis of Multi-VSG System

To analyze the stability of a multi-VSG system,  $I = 2$  is taken as an example. The corresponding structure diagram of a two-VSG system is shown in Figure 9.

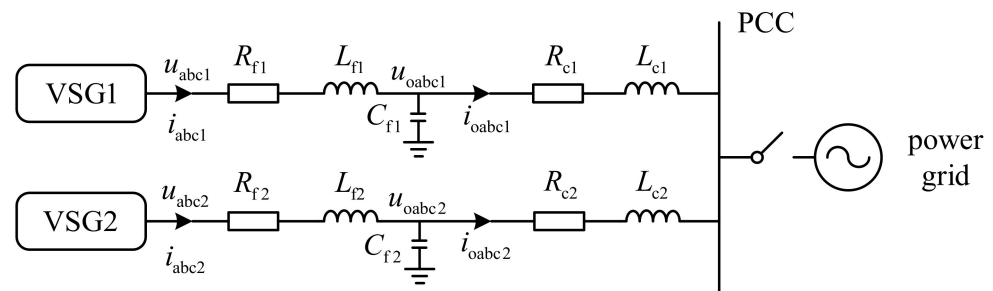


Figure 9. Structure diagram of a two-VSG system.

The system parameters and steady-state operation points are shown in Tables 4 and 5. We bring the parameters in Tables 4 and 5 into Equation (16) to obtain all eigenvalues, as shown in Table 6.

Table 4. Multi-VSG system parameters.

Parameter	Value	Parameter	Value
$R_{f1,2}/\Omega$	0.2	$P_{ref1}/kW$	10
$L_{f1,2}/mH$	3.2	$J_{1,2}$	10
$C_{f1,2}/\mu F$	100	$D_{1,2}$	70
$R_{c1,2}/\Omega$	0.1	$K_{d1,2}$	30
$L_{c1,2}/mH$	1.8	$K_{q1,2}$	0.0005
$P_{ref2}/kW$	13	$K_{pv}$	2
$K_{iv}$	50	$K_{pc}$	7
$K_{ic}$	75		

In Table 6, the two-VSG system has 24 eigenvalues, which are distributed in high-, medium-, and low-frequency bands, corresponding to 12 oscillation modes of the system. All eigenvalues are in the left half plane of the complex plane. The two-VSG system is statically stable. Since the eigenvalues  $\lambda_{1-2}$  are the farthest from the imaginary axis among all eigenvalues and have the largest damping ratio, their influences on the stability of

the system can be ignored. The eigenvalues  $\lambda_{3-12}$ ,  $\lambda_{13-18}$ , and  $\lambda_{19-24}$  correspond to high-, medium-, and low-frequency bands, respectively. By calculating the participation factor, high- and medium-frequency eigenvalues  $\lambda_{3-18}$  are mainly related to the inverter output current controlled by the VSG and the state variables of the LC filter. Low-frequency eigenvalues  $\lambda_{19-24}$  are related to the virtual angular frequency of each VSG and the phase difference with reference coordinates.

**Table 5.** Steady-state operating points of the multi-VSG system.

Parameter	Value	Parameter	Value
$I_{d1}/A$	21.24	$I_{d2}/A$	27.64
$U_{od1}/V$	311.70	$U_{od2}/V$	311.90
$I_{od1}/A$	21.38	$I_{od2}/A$	27.78
$I_{q1}/A$	13.36	$I_{q2}/A$	14.05
$U_{oq1}/V$	4.41	$U_{oq2}/V$	4.41
$I_{oq1}/A$	3.43	$I_{oq2}/A$	4.12

**Table 6.** Multi-VSG system eigenvalues.

Eigenvalue	Real Part	Imaginary Part	Oscillation Frequency/Hz	Damping Ratio	Dominant Related State Variables
$\lambda_{1-2}$	-55129.01	$\pm 319.24$	50.03	0.99	$i_{odq1}, i_{odq2}$
$\lambda_{3-4}$	-1268.41	$\pm 4247.55$	676.36	0.29	$u_{odq1}, u_{odq2}, i_{dq1}, i_{dq2}$
$\lambda_{5-6}$	-937.89	$\pm 1537.41$	244.81	0.52	$u_{odq1}, u_{odq2}, i_{odq1}, i_{odq2}$
$\lambda_{7-8}$	-41.48	$\pm 848.78$	135.16	0.05	$u_{odq1}, u_{odq2}, i_{odq1}, i_{odq2}$
$\lambda_{9-10}$	-33.72	$\pm 3247.69$	517.15	0.01	$u_{odq1}, u_{odq2}, i_{dq1}, i_{dq2}$
$\lambda_{11-12}$	-29.00	$\pm 2340.81$	372.74	0.02	$u_{odq1}, u_{odq2}, i_{dq1}, i_{dq2}$
$\lambda_{13-14}$	-122.46	$\pm 542.93$	86.45	0.22	$i_{odq1}, i_{odq2}$
$\lambda_{15-16}$	-69.26	$\pm 331.68$	52.81	0.21	$i_{odq1}, i_{odq2}, i_{dq1}$
$\lambda_{17-18}$	-60.38	$\pm 336.65$	53.6	0.18	$i_{odq1}, i_{odq2}, i_{dq2}$
$\lambda_{19-20}$	-4.03	$\pm 1.12$	0.18	0.96	$\omega_1, \omega_2$
$\lambda_{21-22}$	-3.2	$\pm 3.17$	0.50	0.71	$\theta_2, \omega_1, \omega_2, \delta_g$
$\lambda_{23-24}$	-4.39	$\pm 2.17$	0.35	0.89	$\theta_2, \omega_1, \omega_2$

### 5.2.2. Influence of Virtual Inertia on Eigenvalues

The change trends of the eigenvalue trajectories of the system with the increase in the virtual inertia of each VSG ( $J = 3.5 \rightarrow 14$ ) are shown in Figure 10. The eigenvalues  $\lambda_{19-24}$  move towards the imaginary axis, and their impact on the system stability cannot be ignored. The eigenvalues  $\lambda_{19-20}$  (green trajectories in the figure) and the eigenvalues  $\lambda_{21-22}$  (blue trajectories in the figure) have the same change trend. When the virtual moment of inertia  $J$  increases to a certain extent, the eigenvalues move away from the real axis and close to the imaginary axis, and the speed away from the real axis is greater than the speed close to the imaginary axis. The eigenvalues  $\lambda_{23-24}$  monotonically and rapidly move away from the real axis and close to the imaginary axis, and the speed close to the imaginary axis is greater than that away from the real axis. The damping of the corresponding oscillation attenuation mode decreases rapidly, and the system stability will worsen.

### 5.2.3. Influence of Damping Coefficient on Eigenvalues

The influence of the change in damping coefficient on the eigenvalue trajectories of the system is shown in Figure 11. With the increase in the damping coefficient of each VSG ( $D = 70 \rightarrow 130$ ), the system eigenvalues in the low-frequency band  $\lambda_{19-24}$  move to the left of the complex plane. The imaginary parts of the eigenvalues  $\lambda_{19-20}$  (green trajectories in the figure) and  $\lambda_{21-22}$  (blue trajectories in the figure) gradually move close to the real axis, and the oscillation frequency of the corresponding oscillation attenuation mode decreases. When the damping coefficient  $D$  increases to a certain extent, they will move away from the imaginary axis and close to the imaginary axis along the real axis. The eigenvalues  $\lambda_{23-24}$  quickly move away from the imaginary axis and close to the real axis. The damping

of the corresponding oscillation attenuation mode increases and the system stability will be improved.

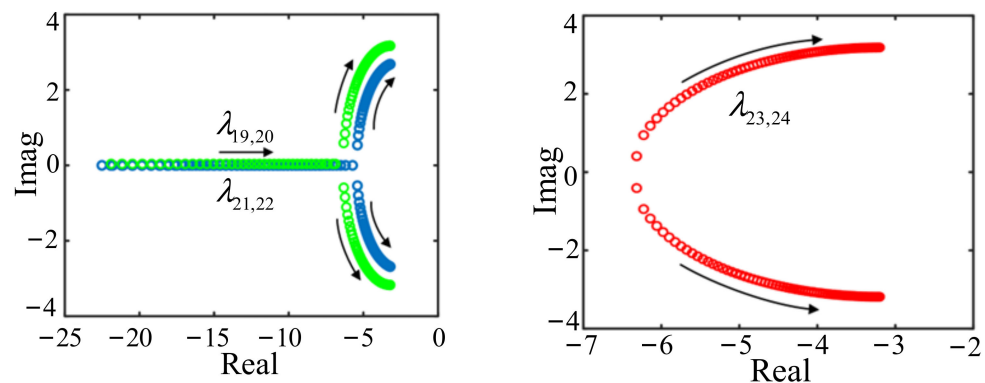


**Figure 10.** Eigenvalue trajectories of system under different virtual inertias.

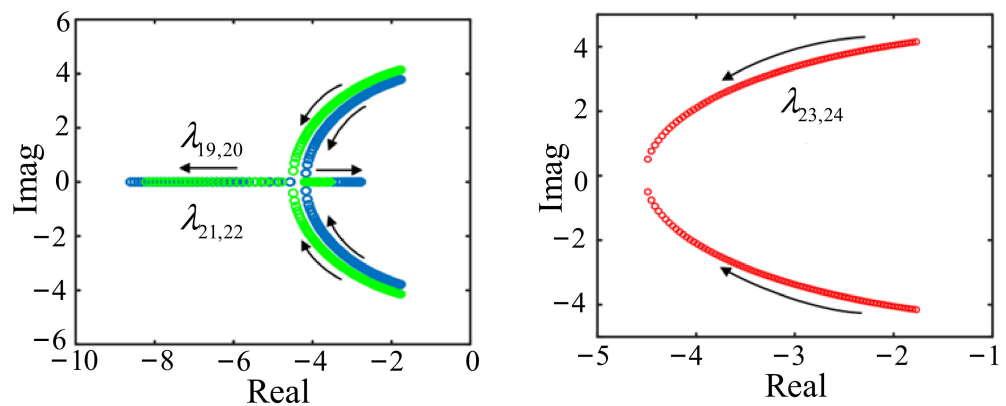


**Figure 11.** Eigenvalue trajectories of the system under different damping coefficients.

#### 5.2.4. Influence of Line Resistance on Eigenvalues

The influence of the line resistance changes on the eigenvalue trajectories of the system is shown in Figure 12. When the line resistance  $R_c$  gradually increases from  $0.025 \Omega$  to  $1 \Omega$ , and other parameters remain unchanged, the high-frequency eigenvalues  $\lambda_{9-12}$  and intermediate-frequency eigenvalues  $\lambda_{15-18}$  move to the left of the complex plane. The moving speeds of the eigenvalues  $\lambda_{9-10}$  are greater than those of the eigenvalues  $\lambda_{11-12}$ . However, the moving speed of the eigenvalues  $\lambda_{15-16}$  (yellow trajectories in the figure) is basically the same as that of the eigenvalues  $\lambda_{17-18}$  (red trajectories in the figure), their imaginary part is basically unchanged, the real part is gradually reduced, and the damping of the corresponding oscillation attenuation mode increases. Therefore, increasing the line resistance can increase the system damping and improve the system stability.

#### 5.2.5. Influence of Line Inductance on Eigenvalues

The influence of line inductance changes on the system eigenvalue trajectories is shown in Figure 13 (yellow trajectories in the figure are eigenvalues  $\lambda_{15-16}$ , red trajectories in the figure are eigenvalues  $\lambda_{17-18}$ ). When the line inductance changes  $L_c = 0.36 \text{ mH} \rightarrow 15 \text{ mH}$ , other parameters remain unchanged, and the intermediate-frequency eigenvalues  $\lambda_{15-18}$  move to the right of the complex plane. The imaginary parts of the eigenvalues  $\lambda_{15-18}$  decrease slowly, the real parts increase rapidly, and the intermediate frequency damping decreases. The low-frequency eigenvalues  $\lambda_{19-22}$  move towards the direction close to the real axis, the real parts of the eigenvalues are basically unchanged, the imaginary parts decrease rapidly, and the oscillation frequency decreases significantly. When the line inductance increases to a certain extent, the eigenvalues move along the right side of the real axis complex plane and quickly approach the imaginary axis, and the low-frequency damping of the system

decreases. Increasing the line inductance can reduce the system damping, which is not conducive to the system's stability.

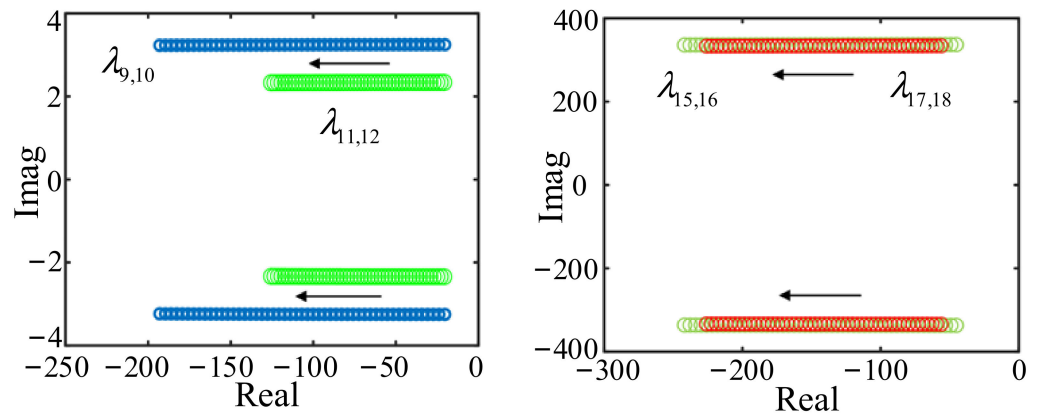


Figure 12. Eigenvalue trajectories of the system under different line resistances.

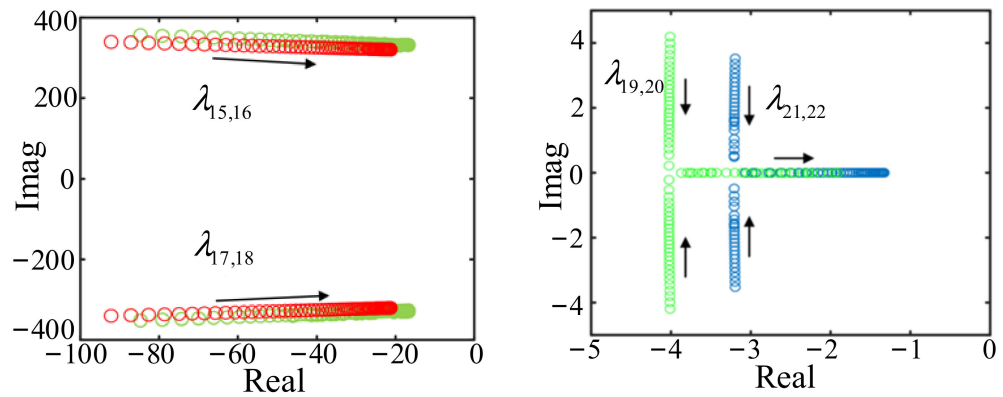


Figure 13. Eigenvalue trajectories of the system under different line inductances.

## 6. Time Domain Simulation Verification and Result Discussion

### 6.1. Simulation of Single-VSG Grid-Connected System

To verify the correctness of the analysis of the above variable parameters on the change law of eigenvalue trajectories, a time domain simulation model of a VSG grid-connected system was built, as shown in Figure 1. The system parameters under the initial operating conditions are shown in Table 1. When  $t = 3$  s, the system load is increased by 2 kW.

Under the initial operating conditions, the system parameters are set as the references. The ratios of the virtual inertia  $J$ , the virtual damping coefficient  $D$ , and the resistance inductance ratio  $r$  of the connecting lines to their corresponding references are 0.5, 1, and 1.5, respectively.

Virtual inertia  $J$  has a significant influence on the active power and virtual angular frequency of the system. As the virtual inertia gradually increases, the overshoot in active power increases, while the overshoot in virtual angular frequency decreases, and the response time and decay oscillation time of active power and virtual angular frequency are extended.

As the virtual damping coefficient increases, the response times of active power and virtual corner frequency remain the same. However, their overshoot is decreased, the oscillation time becomes shorter, and the decay oscillation time becomes faster.

As the resistive inductance ratio  $r$  increases, the response times of active power and virtual angular velocity increase, and the decay oscillation time decreases. The overshoot of active power is decreased, but the overshoot of virtual angular frequency is increased.

6.2. Simulation of Multi-VSG Grid-Connected System

The time domain simulation model of the two-VSG grid-connected system is built to verify the correctness of the analysis of the influence of the above variable parameters ( $J$ ,  $D$ ,  $R_c$ ,  $L_c$ ) on the system stability. With the same other parameters (as shown in Table 4), when the power is disturbed, the response simulation waveforms under different virtual moments of inertia, virtual damping coefficients, line resistances, and line inductances are shown in Figures 14–17, respectively.

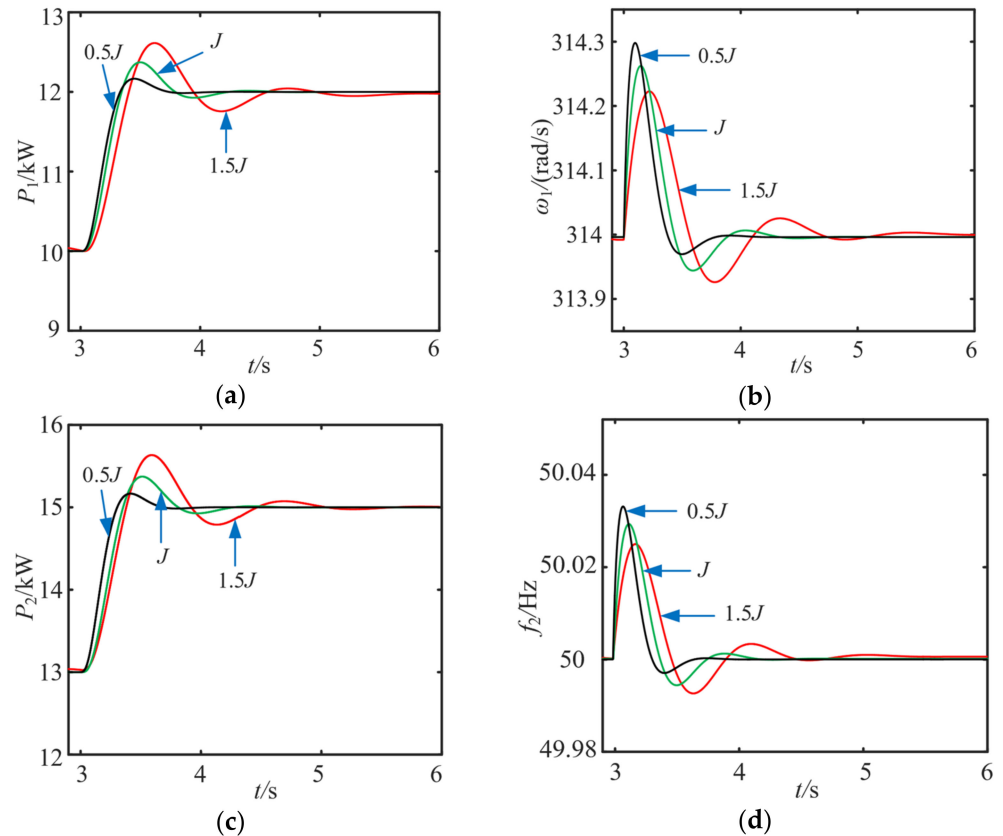


Figure 14. Simulation waveforms with different virtual inertias: (a) active power of VSG1; (b) virtual angular frequency of VSG1; (c) active power of VSG2; (d) frequency of VSG2.

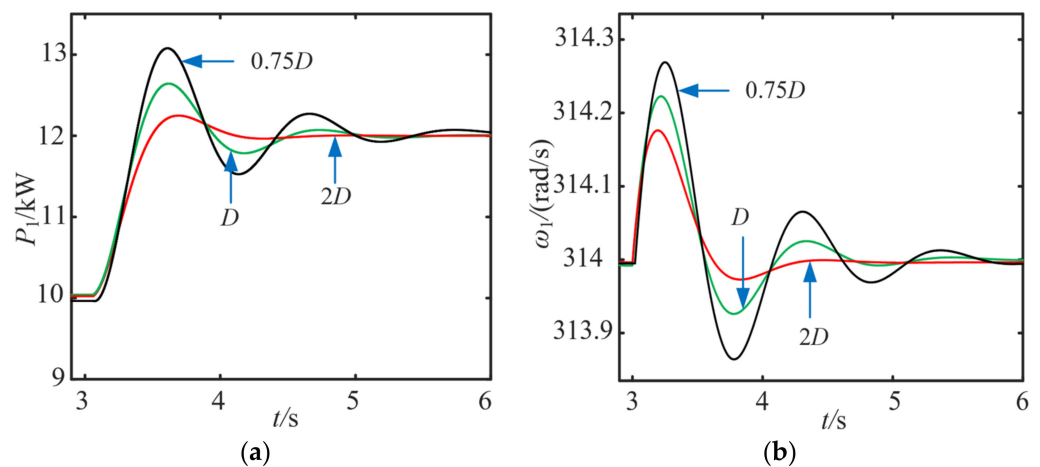
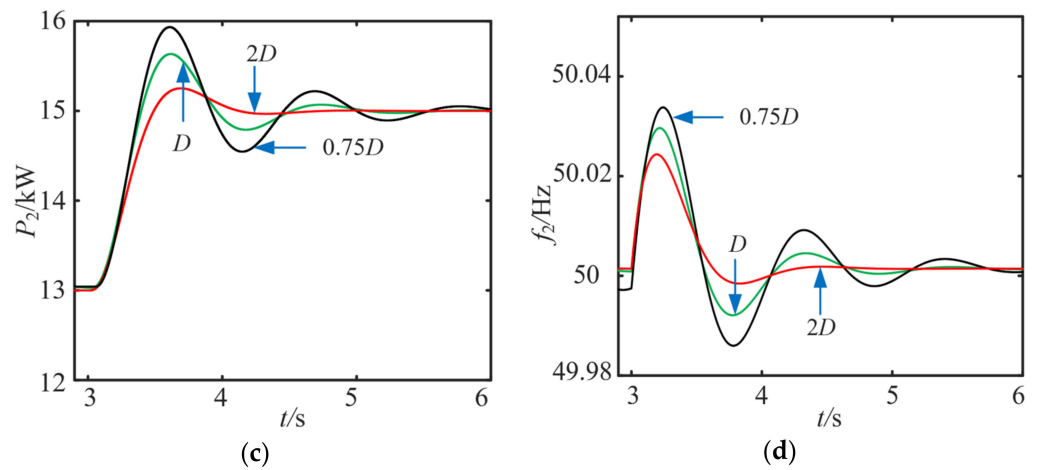
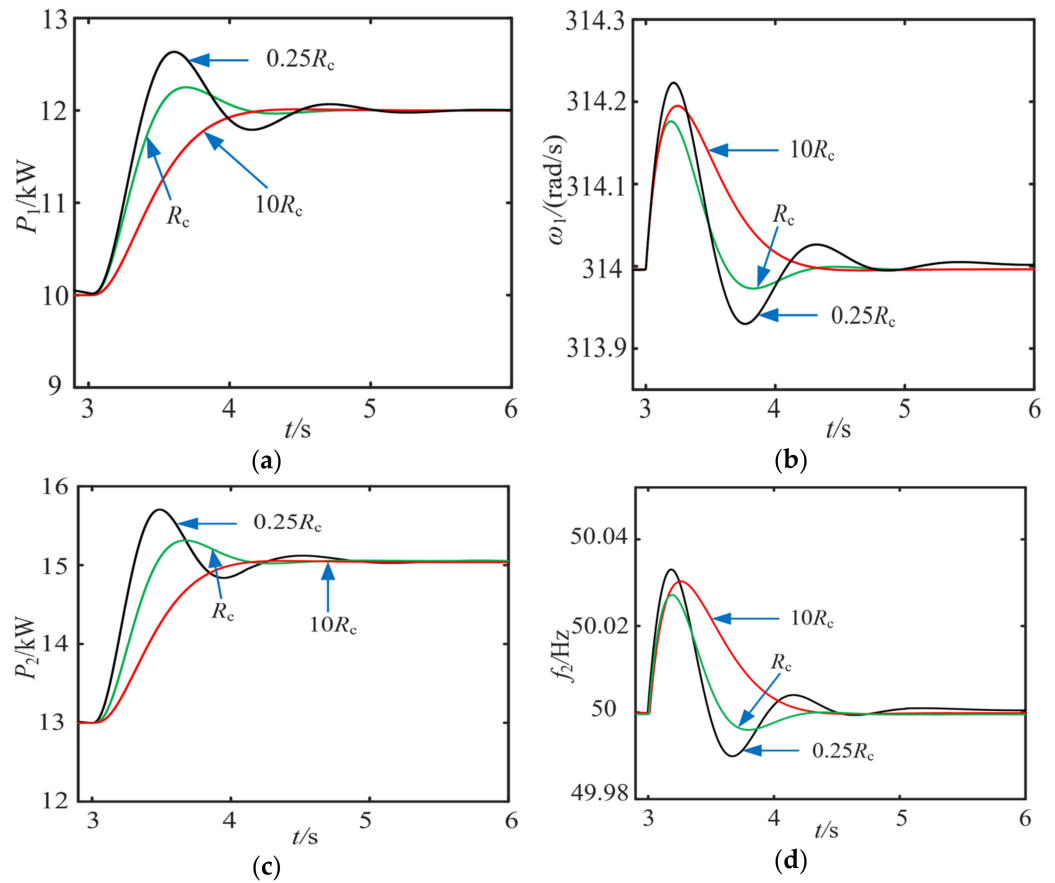


Figure 15. Cont.



**Figure 15.** Simulation waveforms with different damping coefficients: (a) active power of VSG1; (b) virtual angular frequency of VSG1; (c) active power of VSG2; (d) frequency of VSG2.



**Figure 16.** Simulation waveforms with different line resistances: (a) active power of VSG1; (b) virtual angular frequency of VSG1; (c) active power of VSG2; (d) frequency of VSG2.

As can be seen from Figures 14 and 15, increasing the virtual inertia  $J$  or decreasing the virtual damping coefficient  $D$  will make the system unstable under a power disturbance. Increasing the virtual inertia  $J$  influences the number of oscillations of active power and frequency under power disturbance, increasing the regulation time of the system. Increasing the virtual damping coefficient  $D$  reduces the amplitude of oscillations of active power and frequency and shortens the time for the system to reach stability.

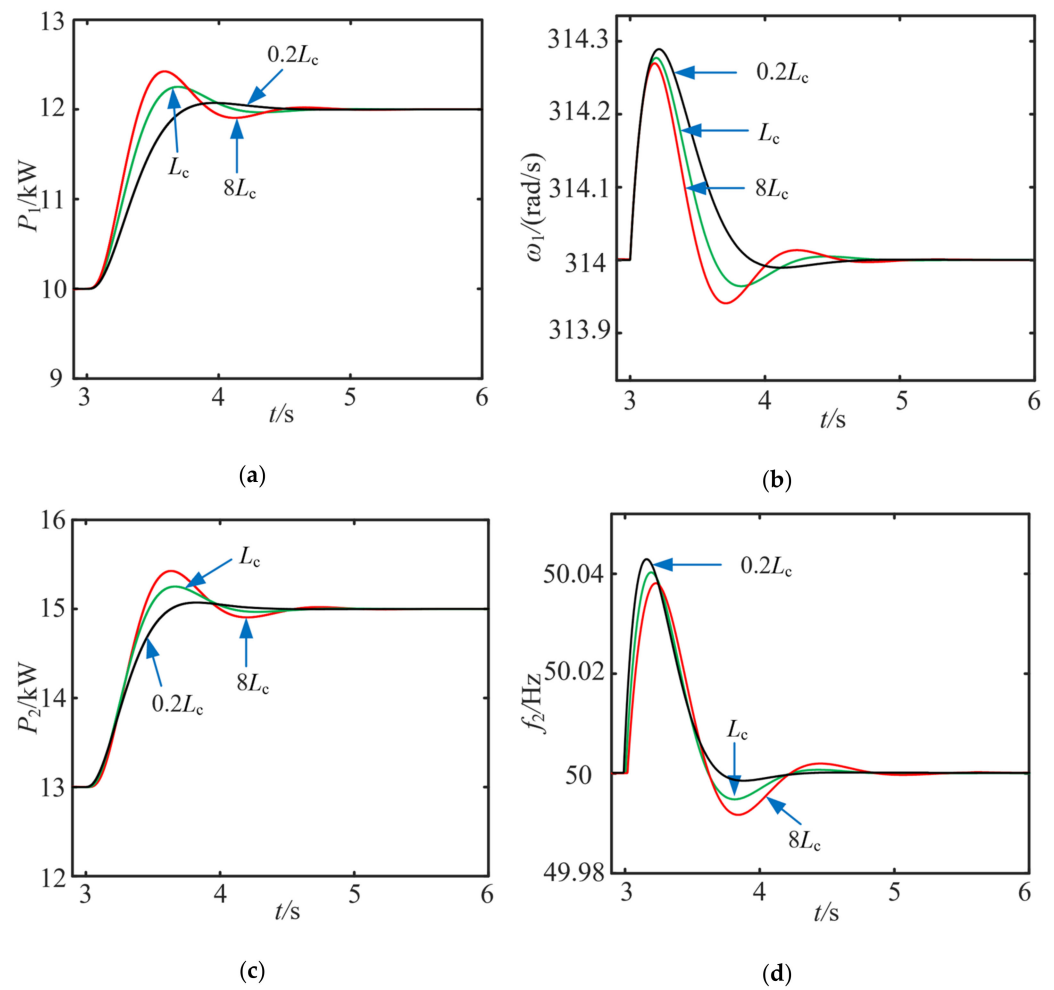


**Figure 17.** Simulation waveforms with different line inductances: (a) active power of VSG1; (b) virtual angular frequency of VSG1; (c) active power of VSG2; (d) frequency of VSG2.

In Figures 16 and 17, reducing the line resistance  $R_c$  or increasing the line inductance  $L_c$  will deteriorate the system stability. Reducing the line resistance  $R_c$  will increase the overshoot of active power, and the adjustment time of active power and frequency will be increased. Increasing the line inductance  $L_c$  will enlarge the overshoot of active power and reduce the overshoot of frequency.

## 7. Conclusions

We studied the stability of single-VSG and multi-VSG systems. The influence mechanisms of various parameters on system stability were verified by small-signal models and numerous simulation models. The conclusions are as follows.

(1) In the single-VSG grid-connected system, increasing the virtual moment of inertia will rapidly reduce the damping ratio of the corresponding oscillation attenuation mode and deteriorate the system stability. Increasing the virtual damping coefficient and the resistance inductance ratio of the connecting line will increase the damping ratio and improve the system stability.

(2) In the multi-VSG system, increasing the damping coefficient and line resistance will increase the system damping and improve the system stability. Increasing the virtual moment of inertia and line inductance will reduce the system damping, which is not conducive to the system stability.

We achieved some research results that provide a theoretical reference for the matching and selection of various parameters in VSG single-machine grid-connected systems

and multi-VSG parallel grid-connected systems. However, further in-depth research and discussion are still needed:

(1) The influence of grid voltage fluctuation is not considered in the small-signal stability analysis of VSG single-machine and multi-machine parallel systems. When the voltage fluctuates, the transient stability of VSG needs further study.

(2) This paper mainly verifies the theoretical analysis through time domain simulation, and a semi-physical test platform based on theory and simulation is necessary to further prove the effectiveness of the results.

**Author Contributions:** Conceptualization, S.L.; Data curation, Y.Z.; Methodology, L.D.; Supervision, Y.S.; Writing—original draft, S.L., L.D., Y.H. and S.C.; Writing—review & editing, J.Y., G.N., G.Z., W.Z. All authors have read and agreed to the published version of the manuscript.

**Funding:** This work was supported by Science and Technology Project of State Grid Liaoning Electric Power Supply Co., Ltd. (2021YF-82).

**Conflicts of Interest:** The authors declare that they have no conflict of interest to report regarding the present study.

## References

- Du, W.J.; Fu, Q.; Wang, H.F. Damping torque analysis of DC voltage stability of an MTDC network for the wind power delivery. *IEEE Trans. Power Deliv.* **2020**, *35*, 324–338. [\[CrossRef\]](#)
- Liu, C.L.; Li, D.Z.; Wang, L.C.; Li, L.; Wang, K. Strong robustness and high accuracy remaining useful life prediction on supercapacitors. *APL Mater.* **2022**, *10*, 061106. [\[CrossRef\]](#)
- Yi, Z.X.; Zhao, K.; Sun, J.R.; Wang, L.; Wang, K.; Ma, Y. Prediction of the remaining useful life of supercapacitors. *J. Power Sources* **2022**, *2022*, 7620382. [\[CrossRef\]](#)
- Li, D.Z.; Li, S.; Zhang, S.; Sun, J.; Wang, L.; Wang, K. Aging state prediction for supercapacitors based on heuristic kalman filter optimization extreme learning machine. *Energy* **2022**, *250*, 123773. [\[CrossRef\]](#)
- Zarifakis, M.; Coffey, W.T.; Kalmykov, Y.P. Active damping of power oscillations following frequency changes in low inertia power systems. *IEEE Trans. Power Syst.* **2019**, *34*, 4984–4992. [\[CrossRef\]](#)
- Wu, W.H.; Chen, Y.D.; Zhou, L.M.; Luo, A.; Zhou, X.P.; He, Z.X.; Yang, L.; Xie, Z.W.; Liu, J.M.; Zhang, M.M. Sequence impedance modeling and stability comparative analysis of voltage-controlled VSGs and current-controlled VSGs. *IEEE Trans. Ind. Electron.* **2019**, *66*, 6460–6472. [\[CrossRef\]](#)
- Khajehoddin, S.A.; Karimi-Ghartemani, M.; Ebrahimi, M. Grid-supporting inverters with improved dynamics. *IEEE Trans. Ind. Electron.* **2019**, *65*, 3655–3667. [\[CrossRef\]](#)
- Zhong, Q.C.; Weiss, G. Synchronverters: Inverters that mimic synchronous generators. *IEEE Trans. Ind. Electron.* **2011**, *58*, 1259–1267. [\[CrossRef\]](#)
- Liu, J.; Miura, Y.; Bevrani, H.; Ise, T. Enhanced virtual synchronous generator control for parallel inverters in microgrids. *IEEE Trans. Smart Grid* **2017**, *8*, 2268–2277. [\[CrossRef\]](#)
- Xu, Y.; Nian, H.; Hu, B. Impedance modeling and stability analysis of VSG controlled type-IV wind turbine system. *IEEE Trans. Energy Convers.* **2021**, *36*, 3438–3448. [\[CrossRef\]](#)
- Baruwa, M.; Fazeli, M. Impact of virtual synchronous machines on low-frequency oscillations in power systems. *IEEE Trans. Power Syst.* **2021**, *36*, 1934–1946. [\[CrossRef\]](#)
- Shuai, Z.K.; Shen, C.; Liu, X.; Li, Z.; Shen, Z.J. Transient angle stability of virtual synchronous generators using lyapunov's direct method. *IEEE Trans. Smart Grid* **2019**, *10*, 4648–4661. [\[CrossRef\]](#)
- Xiong, X.L.; Wu, C.; Blaabjerg, F. Effects of virtual resistance on transient stability of virtual synchronous generators under grid voltage sag. *IEEE Trans. Ind. Electron.* **2022**, *69*, 4754–4764. [\[CrossRef\]](#)
- Liu, H.; Sun, D.W.; Song, P.; Cheng, X.; Zhao, F.; Tian, Y. Influence of virtual synchronous generators on low frequency oscillations. *CSEE J. Power Energy Syst.* **2022**, *8*, 1029–1038.
- Wang, G.Y.; Fu, L.J.; Hu, Q.; Ma, F.; Liu, C.; Lin, Y. Low frequency oscillation analysis of VSG grid-connected system. In Proceedings of the 2021 3rd Asia Energy and Electrical Engineering Symposium (AEEES), Chengdu, China, 26–29 March 2021; pp. 631–637.
- Qin, B.S.; Xu, Y.H.; Yuan, C.; Jia, J. A unified method of frequency oscillation characteristic analysis for multi-VSG grid-connected system. *IEEE Trans. Power Deliv.* **2022**, *37*, 279–289. [\[CrossRef\]](#)
- Alipoor, J.; Miura, Y.; Ise, T. Stability assessment and optimization methods for microgrid with multiple VSG units. *IEEE Trans. Smart Grid* **2018**, *9*, 1462–1471. [\[CrossRef\]](#)
- Choopani, M.; Hosseinian, S.H.; Vahidi, B. New transient stability and LVRT improvement of multi-VSG grids using the frequency of the center of inertia. *IEEE Trans. Power Syst.* **2020**, *35*, 527–538. [\[CrossRef\]](#)

19. Fu, S.Q.; Sun, Y.; Li, L.; Liu, Z.; Han, H.; Su, M. Power oscillation suppression of multi-VSG grid via decentralized mutual damping control. *IEEE Trans. Ind. Electron.* **2022**, *69*, 10202–10214. [[CrossRef](#)]
20. Shi, M.X.; Chen, X.; Zhou, J.Y.; Chen, Y.; Wen, J.Y.; He, H. Frequency restoration and oscillation damping of distributed VSGs in microgrid with low bandwidth communication. *IEEE Trans. Smart Grid* **2021**, *12*, 1011–1021. [[CrossRef](#)]
21. Hu, Y.; Bu, S.Q.; Zhang, X.; Chung, C.Y.; Cai, H. Connection between damping torque analysis and energy flow analysis in damping performance evaluation for electromechanical oscillations in power systems. *J. Mod. Power Syst. Clean Energy* **2022**, *10*, 19–28. [[CrossRef](#)]